Accepted Manuscript

Energetic helical electron-bunch generation driven by a light spring wakefield

Rongxuan Liu [1], Xiaomei Zhang[1,¯], Yuanxin Chang[1], Jicheng Liu[1], Baifei Shen [1,=] and Zhangli Xu[1]

[1] *Department of physics, Shanghai Normal University, Shanghai 200234, China*

Abstract This paper investigates the interaction between a light spring pulse and a gaseous plasma, resulting in the formation of a three-dimensional helical wakefield and the generation of a high-energy helical electron beam carrying orbital angular momentum (OAM). During this process, the ponderomotive force of the LS expels background electrons along helical trajectories, forming a unique "spring-like" bubble structure. Within this bubble, not only does a longitudinal acceleration field exist, imparting longitudinal momentum to the injected electrons, but also the synergistic interplay between the azimuthal electric and radial focusing fields endows the trapped and accelerated electrons with significant OAM. Most importantly, the OAM and helical structure of the electron beam are well-preserved even after propagation into the vacuum. This paper reveals that the spring-like wakefield driven by an LS pulse serves as a novel acceleration structure. This creates a new pathway for the direct generation of high-energy electron beams that carry OAM and exhibit three-dimensional structural characteristics. Furthermore, it expands the potential application prospects of this beams in advanced fields such as radiation sources and the detection of materials sensitive to angular momentum.

Keywords: light spring; wakefield; electron beams; orbital angular momentum.

¯ Author to whom correspondence should be addressed. Electronic mail: zhxm@shnu.edu.cn
= Author to whom correspondence should be addressed. Electronic mail: bfshen@shnu.edu.cn

This peer-reviewed article has been accepted for publication but not yet copyedited or typeset, and so may be subject to change during the production process. The article is considered published and may be cited using its DOI.

This is an Open Access article, distributed under the terms of the Creative Commons Attribution licence (https://creativecommons.org/licenses/by/4.0/), which permits unrestricted re-use, distribution, and reproduction in any medium, provided the original work is properly cited.

10.1017/hpl.2026.10192

https://doi.org/10.1017/hpl.2026.10192 Published online by Cambridge University Press

1. Introduction

With the rapid advancement of high-power laser technology, the performance parameters of laser driven electron beams have been significantly improved [1]. On the one hand, the increasing laser intensity enables electrons to be accelerated to the GeV level and beyond [2-5]. On the other hand, the continuous development of optical vortex technology [6-10] has laid an important foundation for generating helical electron beams using high-power lasers. In contrast to conventional electron beams, helical electron beams possess a spatial structure and typically carry orbital angular momentum (OAM) [11-14]. They have significant applications in physics and various other fields, including materials science [15], quantum information technology [16], and advanced accelerators [17-19].

Recent breakthroughs in laser-driven electron acceleration are primarily based on wakefields [20-22] generated by the interaction between high-power laser pulses and plasma. The acceleration mechanism of wakefields driven by conventional Gaussian beams has been extensively studied. The approximately spherical wakefield excited by an intense Gaussian laser not only possesses an extremely high longitudinal acceleration gradient but also produces a significant transverse focusing effect on the accelerated electrons. Its acceleration gradient can reach 100 GV/m, thereby enabling electrons to gain energy on the GeV scale over centimeter-scale distances. In contrast, an optical vortex beam carrying OAM, such as a Laguerre–Gaussian (LG) beam, can drive the formation of a donut-like bubble structure with a central electron column [23-29]. The transverse electric field within this structure exhibits a strong focusing effect on positive charges, making it particularly suitable for accelerating positively charged particles such as positrons and protons.

Recently, a novel type of coupled helical light beam, known as a light spring (LS) [30], which has both a spiral phase structure and helical intensity profile, has attracted increasing interest. This beam introduces new geometric and topological degrees of freedom into laser-plasma interactions. The LS exhibits chirped characteristics in both its frequency and topological charge, demonstrating potential applications in suppressing laser-plasma instabilities and enhancing the efficiency of particle acceleration [31]. The advantage of the LS lies not only in its OAM but also, more importantly, in its unique spatiotemporally coupled structure. This structure enables the laser energy to be highly concentrated in the azimuthal direction, thereby generating an extremely

https://doi.org/10.1017/hpl.2026.10192 Published online by Cambridge University Press

high peak intensity during interaction with a gaseous plasma and driving the formation of an extremely strong accelerating wakefield.

Recent studies have shown that when the peak power of a LS reaches the petawatt level, it can effectively accelerate protons [32]. In contrast, electrons have a much lighter mass than protons, enabling injection and significant energy gain at relatively lower laser powers. Furthermore, because the driving laser pulse carries orbital angular momentum and exhibits a helical intensity distribution characteristic of a LS, this feature is expected to be transferred to the electrons. Vieira et al. first proposed the theoretical framework in which a LS synthesized from two LG beams excites a twisted wakefield, and showed via the Panofsky-Wenzel theorem that electrons acquire a quantized orbital angular momentum in proportion to their longitudinal momentum gain [33]. Motivated by this pioneering work, the present study provides original contributions to electron acceleration: we adopt a seven-LG-beam superposition scheme to construct a LS, focus on the wakefield bubble structure, examine the structural preservation of the helical electron beam after it exits the plasma into vacuum, and provide quantifiable performance metrics. Based on this, this paper examines the interaction between a relatively low-intensity LS with a helical-intensity distribution and a gaseous plasma target. The resulting bubble wakefield exhibits a three-dimensional (3D) helical structure, thereby generating a helical electron bunch carrying OAM. Further analysis reveals that the specific distribution of fields within this helical bubble structure is the key factor enabling the electrons to acquire OAM.

2. 3D PIC Simulation results

To study the interaction between the laser pulse and the plasma, we performed 3D particle-in-cell (PIC) simulations using the EPOCH code [34]. The LS is synthesized by superposing multiple LG beams with different topological charges and frequencies. Specifically, each LG beam with a distinct topological charge l_n is associated with a specific frequency ω_n The LS, synthesized from N LG beams, each with a normalized vector potential a_0 and a radial node number p = 0, can be described as

$$A_{LS}(r,\varphi,t) = \sum_{n=1}^{N} a_0 \left(\frac{\sqrt{2}}{w_{zn}}\right)^{|l_n|} \exp\left(-\frac{r^2}{w^2{}_{zn}}\right) \exp[i(l_n\varphi - \omega_n t)] \qquad (1)$$

Here, N is the total number of beams. The beam radius is given by $W_{zn} = W_{0n}\sqrt{(z^2 + z_R{}^2)/(z_R{}^2)}$, where z_R is the Rayleigh length, and W_{0n} is the nominal waist radius of the n-th sub-beam with frequency ω_n and

https://doi.org/10.1017/hpl.2026.10192 Published online by Cambridge University Press

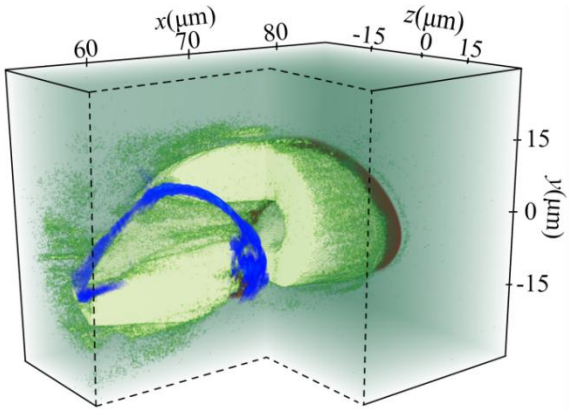
topological charge l_n. The frequency ω_n of each individual sub-beam in the LS satisfies $\omega_n = \omega_1 + \Delta\omega(n-1)$, and the topological charge l_n satisfies $l_n = l_1 + \Delta l(n-1)$. These two parameters fulfill the following relationship: $l_n = l_1 + \Delta l/\Delta\omega(\omega - \omega_1)$. To ensure that the intensity peaks of the LG beams with different topological charges l_n overlap radially when superimposing to form the LS, the waist radius W_{0n} of each LG beam follows $W_{0n} = W_{01}\sqrt{l_1/l_n}$. The specific parameters are listed in Table 1. The LS used in the simulation is synthesized from seven *y*-polarized LG beams with Δl= 1 and topological charges l ranging from 1 to 7. The central wavelength (corresponding to the sub-beam with the average topological charge) is $\lambda_4 = 0.8$ μm, and the normalized peak intensity is $a_0 = eA/m_e c^2$ =1.2. The optical cycle period is T_0= λ_4/c.The waist radius of the first LG beam is $W_{01} = 20$ μm. Its frequency is ω_1= 0.85ω_0, where ω_0 is the central frequency (ω_0= ω_4). The frequency interval between each beam is $\Delta\omega$= $\alpha\omega_0$.α is the dimensionless frequency chirp parameter of the LS, defined as the ratio of the frequency interval between two adjacent LG sub-beams to the central frequency. In this paper,α=0.05. Detailed data for the other LG beams are presented in Table 1. Δt is the temporal pitch of the LS intensity helix, that is, the time interval corresponding to one complete rotation of the helical envelope, and its relationship with the spatial pitch Δx is given by $\Delta x = c\Delta t$. Under these conditions, the pitch of the LS is $\Delta x = 2\pi c/\Delta\omega = 2\pi c/\alpha\omega_0$ =16 μm. The pulse duration is τ = 66.7 fs. The laser beam propagates along the positive x axis. The peak laser intensity is I = 1.5×10^{20} W/cm^2, the total laser power is 71 TW, and the total energy is 4.74 J. The simulation window is divided into 600×400×400 cells, with one particle placed per cell. The dimensions of the moving simulation window are 50 μm (*x*) × 80 μm (*y*) × 80 μm (*z*). The simulation window is divided into 600×400×400 cells, with one macro-particle placed per cell. It should be noted that additional simulation conducted at higher resolutions have verified that the simulation results obtained at the current resolution are well converged. A gaseous plasma (a plasma of gas density) is a pre-ionized electron-proton plasma with a density of 0.008 n_c ($n_c = \varepsilon_0 m_e {\omega_0}^2/e^2$ is the critical plasma density for the central wavelength, for 800 nm, n_c≈1.7×10^{21}cm^{-3}) is introduced in the region defined by 40 μm < x < 130 μm, −38 μm < y < 38 μm, and −38 μm < z < 38 μm.

https://doi.org/10.1017/hpl.2026.10192 Published online by Cambridge University Press

Table 1. Correspondence between the topological charge (l) and the focal spot size (ω_{0n}) for the LG beams composing the LS.

Topological charge (l_n)	1	2	3	4	5	6	7
angular frequency (ω_n)	$0.85\omega_0$	$0.9\omega_0$	$0.95\omega_0$	ω_0	$1.05\omega_0$	$1.1\omega_0$	$1.15\omega_0$
Nominal waist radius (W_{0n}(μm))	20	14.144	11.547	10	8.944	8.165	7.559

The 3D structure of the wakefield driven by the LS in the gaseous plasma is shown in Figure 1. At the forefront of the wakefield structure, the driving LS pulse exhibits a distinct helical intensity distribution (highlighted in red). The wakefield behind the LS pulse exhibits a helical, spring-like structure. This structure is markedly different from the spherical bubble formed by a conventional Gaussian pulse-driven wakefield, and from the quasi-spherical bubble structure typically generated by an LG pulse-driven wakefield. This significant difference results from the distinct manner in which electrons are evacuated by the ponderomotive force during the laser-plasma interaction. The intensity of the LS pulse varies in a spring-like pattern along the propagation direction. As it propagates through the plasma, the ponderomotive force exerted on the electrons is no longer axisymmetric but instead exhibits a helical distribution along the propagation axis. Consequently, electrons are expelled by the ponderomotive force of the laser pulse in a helical manner, whereas the heavier ions remain nearly stationary. Therefore, the electron plasma bubble driven by the LS pulse is a distinct 3D structure with pronounced helical twisting. This helical bubble structure not only mirrors the spatial topological properties of the driving light field but also introduces new degrees of freedom for accelerated electrons. As illustrated in Figure 1, the accelerated electron beam itself exhibits a corresponding spatial helical structure.



https://doi.org/10.1017/hpl.2026.10192 Published online by Cambridge University Press

Figure 1. Wakefield structure, the electron bunch within the wakefield, and the driving LS during its propagation in the plasma at t = 298.7 fs. The background electron density is represented by a green color scale, with darker shades corresponding to higher densities. The bubble is cut away along the dashed line. Blue represents the energetic electron bunch with energy > 5 MeV. Dark red color represents the LS, located at the front of the bubble.

Figure 2(a) presents the electron density map of the longitudinal cross-sections. Figures 2(b) – 2(g) show the transverse cross-sectional distributions of the electron density at different positions where electron injection into the helical bubble structure has already occurred. The structure of the helical bubble driven by the LS pulse is clearly discernible in the cross-sectional density distributions. The regions highlighted by the circles correspond to a high-density electron bunch located within the bubble, which represents the electrons trapped and accelerated in the wakefield. Owing to the intrinsically spring-like 3D structure of the bubble, the bubble length in each cross-section that intersects the central axis and rotates along the helical structure is about λ_p =16 μm, as shown in Figure 2(a) . In each bubble cross-section, the region closer to the laser field is the bubble head, whereas the opposite side is the rear. The positions of the bubble head and rear vary spirally across the different cross-sections. In other words, consecutive bubble cross-sections collectively form a 3D helical bubble structure. During the interaction between the LS pulse and the plasma, when the laser electric field intensity is sufficiently high, the wakefield inside the bubble is sufficiently strong to cause the electrons on the wall of the helical bubble to be continuously injected into the rear region of the bubble. Because the rear part of the bubble varies helically, the continuously injected electrons naturally form a helical, spring-like structure. As the acceleration process continues, the helical electron beam gradually migrates from its initial position near the bubble wall toward the interior of the bubble. This demonstrated the acceleration behavior and a focusing process toward the central spiral region of the bubble in 3D space.

https://doi.org/10.1017/hpl.2026.10192 Published online by Cambridge University Press

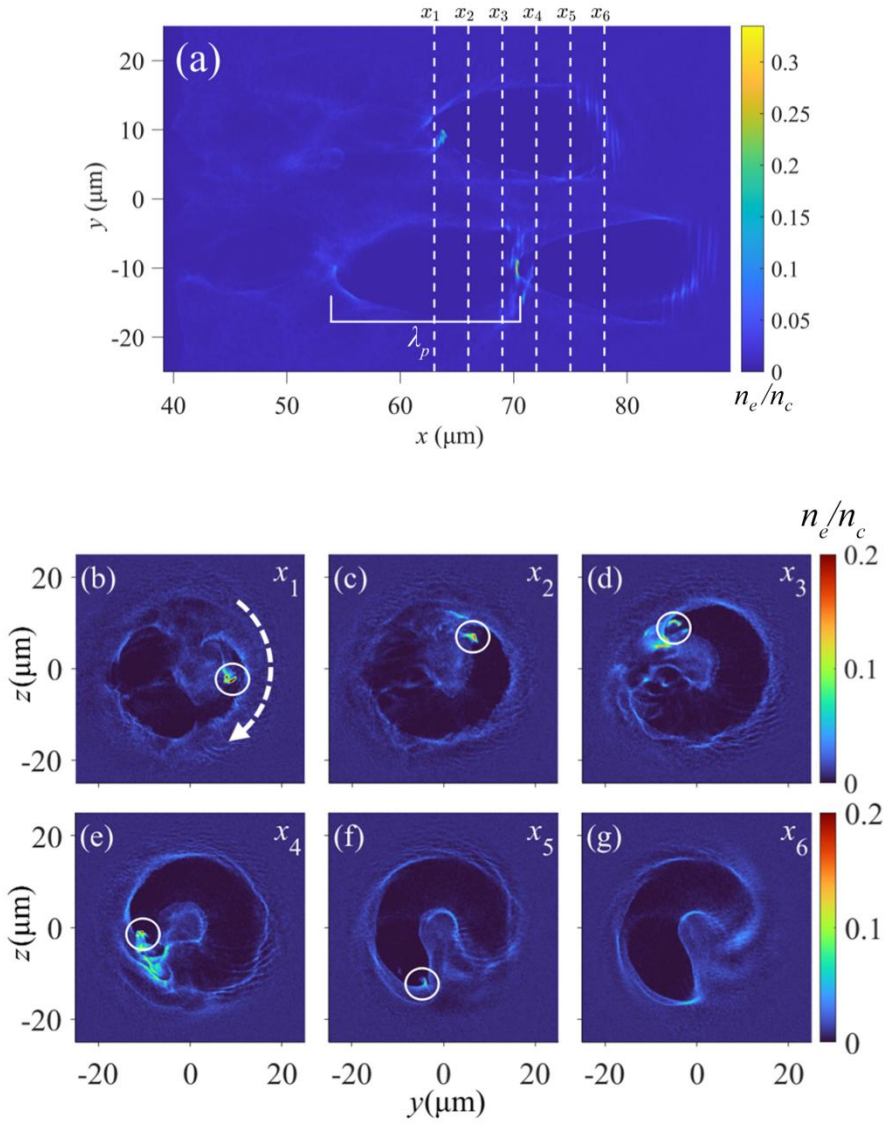


Figure 2. (a) Electron density distribution in the $x-y$ plane at $z = 0$ during the early stage of plasma wakefield acceleration at $t = 298.7$ fs. The length of the white line segment is equal to one bubble size λ_p. (b) – (g) show the density cross-sectional distributions at different x-positions in (a), where (b) corresponds to $x_1 = 63$ μm, (c) to $x_2 = 66$ μm, (d) to $x_3 = 69$ μm, (e) to $x_4 = 72$ μm, (f) to $x_5 = 75$ μm, and (g) to $x_6 = 78$ μm. The high-density electron bunch within the white circles corresponds to the electrons trapped in the LS wakefield. The arrow in (b) indicates the helical direction of the electron bunch when observed moving toward the positive x direction clockwise.

https://doi.org/10.1017/hpl.2026.10192 Published online by Cambridge University Press

Figure 3 shows the moment when the laser and electron beam exit the plasma region and enter the vacuum. The electron bunch in the vacuum maintains a clear helical structure behind the LS. The maximum electron energy is 103 MeV. This high energy portion is located at the front of the helical electron bunch because it is injected earlier and has undergone a longer acceleration process within the bubble. The energy spectrum of this electron beam is shown in Figure 4. the total charge constituting the helical electron bunch is approximately 9.53 nC.

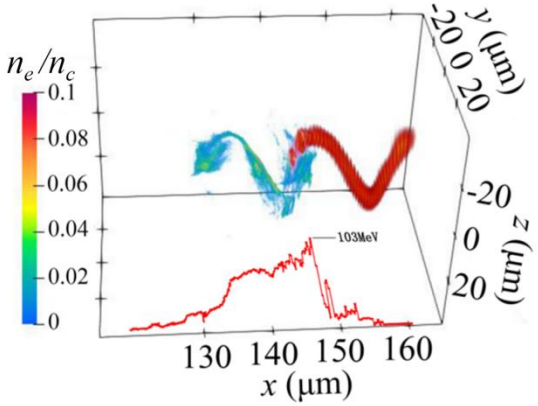


Figure 3. 3D depiction of the electron density for energies > 10 MeV and the electric field strength E_y of the LS at t = 555 fs. The figure illustrates the distribution of the accelerated electron bunch as it is ejected from the plasma (on the left side) and ultimately enters the vacuum completely. The red color represents the driving LS. The colorbar represents the density of electrons with energy E > 10 MeV. The solid red line on the bottom plane connects the points of maximum energy (E) along the x direction.

Calculations show that at the initial moment, the incident LS pulse carries a total x-direction angular momentum of -6.88×$10^{19}\hbar$. By t = 555 fs, for electrons in this bunch with energies exceeding 10 MeV, the total x-direction angular momentum and the average angular momentum per electron are -6.67×$10^{18}\hbar$ and -2.9×$10^{8}\hbar$, respectively. The corresponding angular momentum conversion efficiency is 12.78%, while the energy conversion efficiency is 2.20%. Further calculations at t = 555 fs shows that the transmitted LS pulse carries a total x-direction angular momentum of −5.22×$10^{19}\hbar$, corresponding to a decrease of −1.66×$10^{19}\hbar$ in the laser angular momentum. This loss is distributed as follows: the trapped and accelerated electrons remaining within the simulation window acquire -9.57×$10^{18}\hbar$; protons gain −1.57×$10^{18}\hbar$; and the remaining −5.46 × $10^{18}\hbar$

https://doi.org/10.1017/hpl.2026.10192 Published online by Cambridge University Press

is attributed to electrons that have been accelerated and subsequently exited the simulation boundary as the moving window advances. The above budget analysis clearly demonstrates that the vast majority of the angular momentum lost by the LS pulse is transferred to the plasma particles, with the trapped accelerated electrons accounting for the dominant fraction - approximately 57.6% of the total laser angular momentum loss.

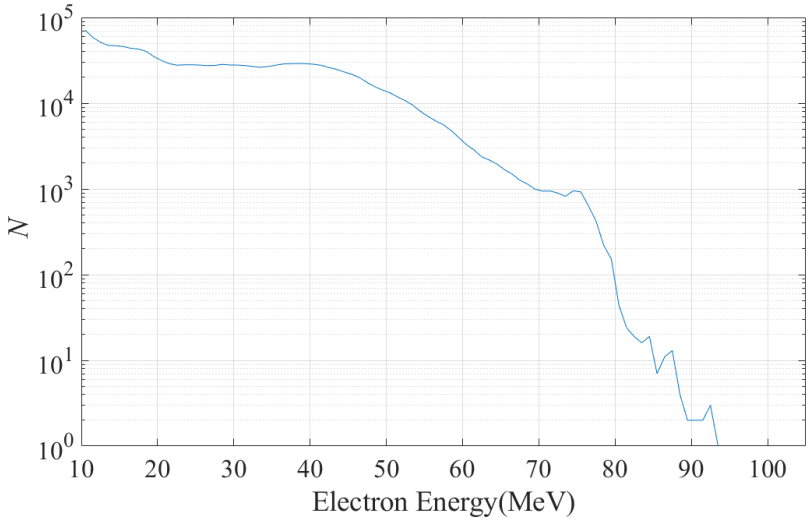


Figure 4. The energy spectrum for energies greater than 10 MeV.

Both energy and OAM are intrinsic properties of the laser field. Within our simulation time window, we have analyzed the temporal evolution of the laser energy and OAM, alongside the energy and OAM of electrons with energies above 10 MeV, as presented in Figure 5. The results clearly show consistent trends: the laser energy decreases while the electron energy increases; the total x-direction OAM of the laser decreases while that of the electrons increases. This consistent behavior provides strong support for the physical mechanism that the laser wakefield transfers the LS OAM to the accelerated electrons.

https://doi.org/10.1017/hpl.2026.10192 Published online by Cambridge University Press

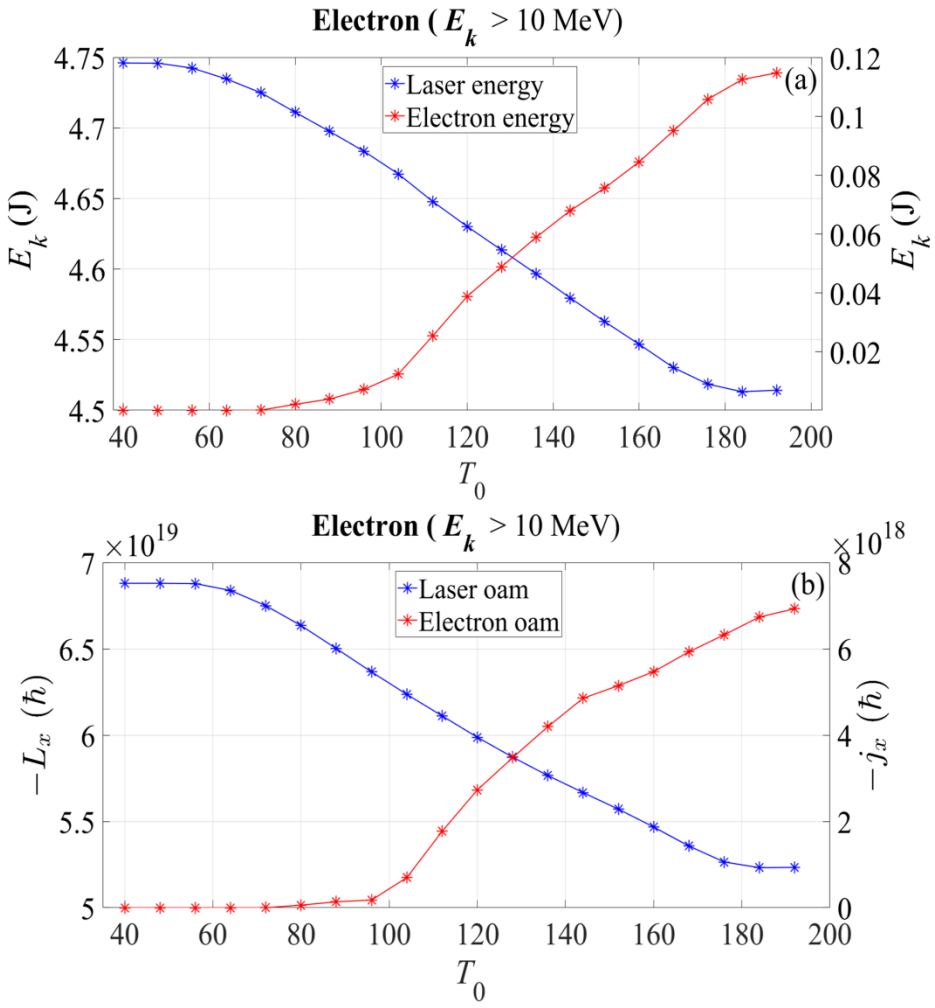


Figure 5. (a) Temporal evolution of the laser energy and the energy of electrons with energies above 10 MeV. (b) Temporal evolution of the laser OAM and the OAM of electrons with energies above 10 MeV. At t=184 T_0, the laser leaves the plasma, and the transfer stops.

The localization of accelerated electrons at the rear of the bubble indicates that the key factor determining the formation of the helical electron beam is primarily governed by the internal electromagnetic field structure of inside the bubble, rather than by the direct influence of the laser field. Figure 6 shows that the longitudinal wakefield E_x driven by the LS exhibits a 3D helical distribution. The trapping of electrons primarily occurs within the negative value region of this longitudinal wakefield, and continuously gain acceleration.

https://doi.org/10.1017/hpl.2026.10192 Published online by Cambridge University Press

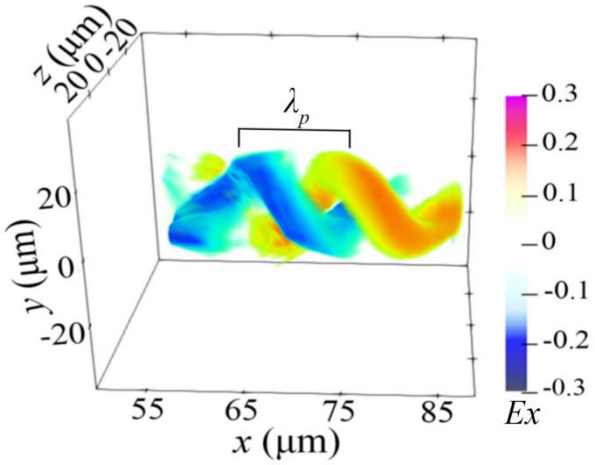


Figure 6. Longitudinal electric field of the wakefield driven by the LS at t = 298.7 fs.

The distribution of the transverse wakefield inside the bubble is shown in Figure 7. Figure 7(a) depicts the radial electric field $\boldsymbol{E_r}$, defined as $\boldsymbol{E_r} = (\boldsymbol{e} \cdot \boldsymbol{E}_\perp) \cdot \boldsymbol{e}$, $\boldsymbol{e} = (\boldsymbol{0}, \boldsymbol{y}/\sqrt{\boldsymbol{y^2 + z^2}}, \boldsymbol{z}/\sqrt{\boldsymbol{y^2 + z^2}}), \boldsymbol{E}_\perp = (0, \boldsymbol{E_y}, \boldsymbol{E_z})$. When viewed from the positive x axis, the positive direction points radially outward. This field exerts a significant transverse focusing effect on the electrons and is a key factor in determining their transverse distribution. In this field, the accelerated electrons can be effectively confined and concentrated toward the helical center of the bubble. Meanwhile, we also note the azimuthal electric field $\boldsymbol{E_\varphi}$ shown in Figure 7(b), defined as $\boldsymbol{E_\varphi} = (\boldsymbol{e} \times \boldsymbol{E}_\perp) \times \boldsymbol{e}$. When viewed from the direction of the positive x axis, the positive direction corresponds to the counterclockwise direction. This field accelerates the injected electrons in the azimuthal direction. As indicated by the electron density in Figure 2(g), the accelerated electrons are located within the positive region of the azimuthal electric field. This results in the rotational acceleration of the electrons in the clockwise direction, thereby endowing them with OAM.

Therefore, the spring-like bubble structure accelerates the electrons longitudinally, enabling their continuous acceleration and energy gain. In the transverse direction, while the radial electric field $\boldsymbol{E_r}$ confines and focuses the electrons, it also places them within an accelerating azimuthal electric field $\boldsymbol{E_\varphi}$, thereby enabling the electrons to acquire OAM. Under the combined action of the longitudinal and transverse fields, the trapped electrons form a helical electron beam that is concentrated around the helical center of the bubble and carries OAM.

https://doi.org/10.1017/hpl.2026.10192 Published online by Cambridge University Press

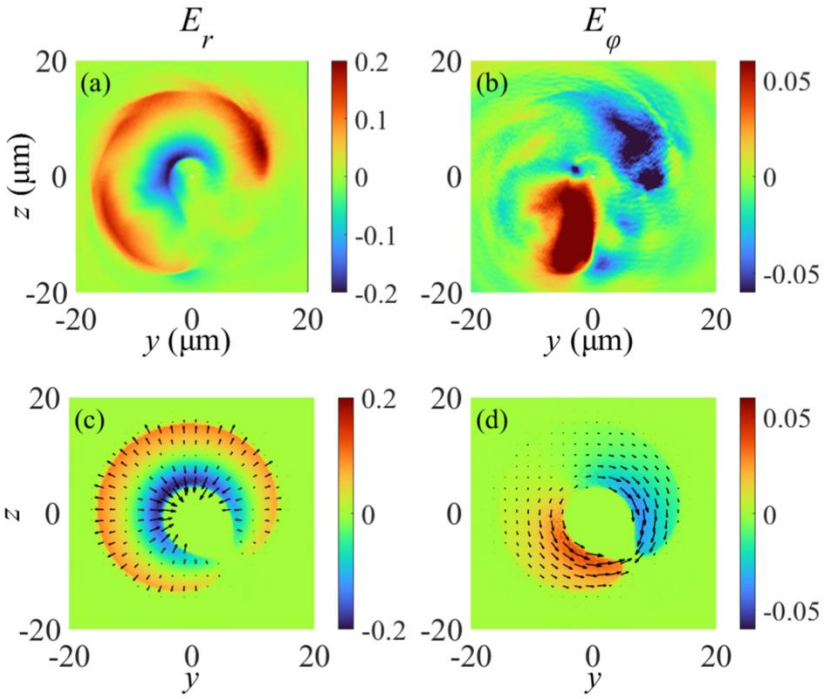


Figure 7. Transverse electric field distribution at the position $x = 78$ μm at $t = 298.7$ fs (corresponding to the density distribution in Figure 2(g)). (a) and (b) show the PIC numerical simulation results, whereas (c) and (d) show the theoretical analytical results. The horizontal and vertical coordinates (y, z) are normalized. (a) and (c) depict the radial electric field component $\boldsymbol{E_r}$, and (b) and (d) depict the azimuthal electric field component $\boldsymbol{E_\varphi}$. The arrows indicate the direction of the electric field.

According to the simulation results, in the transverse direction, the unique spring-like bubble structure generates an azimuthal electric field $\boldsymbol{E_\varphi}$. This field provides azimuthal acceleration to the electrons, thereby enabling them to acquire OAM. In the bubble driven by the LS pulse, the motion of electrons can be likened to traveling through a "spiral-slide-like" acceleration channel, where they gain both longitudinal acceleration and continuous azimuthal acceleration. This process differs significantly from that of a toroidal bubble driven by the LG pulse. The toroidal bubble driven by the LG pulse is axisymmetric and thus lacks structural variation in the transverse plane. Consequently, it cannot form an effective $\boldsymbol{E_\varphi}$ field. In contrast, the helical bubble driven by the LS pulse is not axisymmetric. This vortex-accelerating field structure is a characteristic of an LS-driven wakefield, thereby endowing the accelerated electrons with OAM.

https://doi.org/10.1017/hpl.2026.10192 Published online by Cambridge University Press

Although the above discussion only includes the electric field contribution, it should be noted that the electron dynamics are determined by both the electric field and the $v \times \boldsymbol{B}$ term. For electrons trapped and accelerated to relativistic velocities ($v \approx c$) inside the bubble, the $v \times \boldsymbol{B}$ term in the Lorentz force becomes comparable in magnitude to the electric force. Specifically, the azimuthal component of the electric field $\boldsymbol{E_\varphi}$, and the radial magnetic contribution -$(v \times \boldsymbol{B_r})$ are of the same order and play an equivalent role in driving the azimuthal electron motion that generates the OAM. Likewise, for the radial focusing, $\boldsymbol{E_r}$ and $\left(v \times \boldsymbol{B_\varphi}\right)$ are comparable. This implies that the electric and magnetic fields contribute comparably.

The above discussion is based on PIC simulation results. To elucidate the formation mechanism of helical electrons, we have constructed a theoretical model of a spring-like bubble field (see Appendix). We construct a complex bubble structure and its associated electric field by integrating infinitesimal field elements along a curved path. The cross-section of an infinitely long cylindrical bubble is adopted as a simplified integration element. By integrating this cross-sectional field element along a spring-like helical trajectory, we obtain the electric-field distribution within the spring-like bubble, as shown in Figures 7(c) and 7(d). The transverse field distribution from the theoretical model is in good agreement with the simulation results. This confirms that the field distribution of the helical bubble structure determines the generation of a helical electron beam carrying OAM.

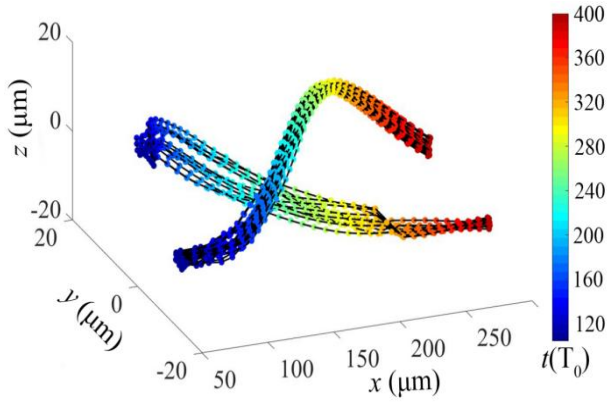


Figure 8. 3D trajectory of electrons with the final momentum of 150 $m_e c$. The colorbar on the right represents different times, and the trajectory is colored according to the propagation time.

The helical wakefield distribution driven by the LS pulse determines the electron beam trajectory. The unique spring-like bubble field structure is key to enabling electrons to acquire OAM. To investigate the motion

https://doi.org/10.1017/hpl.2026.10192 Published online by Cambridge University Press

characteristics of electrons during acceleration, we extended the acceleration distance. While maintaining all other simulation conditions unchanged, we increased the plasma target length in the x direction from 130 to 300μm, enabling the relativistic electron beam to propagate continuously within the bubble. Using a particle-trajectory tracking method, we selected two groups of electrons located at different spatial positions (with different initial transverse positions) within the bubble and tracked their trajectories. The trajectory results are shown in Figure 8. While all the electrons continue to propagate forward along the x direction, they exhibit helical trajectories in the longitudinal plane. The motion of these electrons in the helical wakefield exhibits pronounced 3D gyration characteristics. Furthermore, the figure shows that electrons at different initial positions exhibit slight variations in their gyration periods. This indicates that electrons injected at different positions acquire different energies during acceleration.

In contrast to the electron gyration trajectories in conventional bubbles, the electrons accelerated within the helical bubble driven by the LS pulse exhibit simultaneous propagation along the x direction and rotation in the transverse plane. This azimuthal rotation is a direct result of the acceleration by the azimuthal electric field. Therefore, a betatron radiation source carrying OAM is expected to be obtained from such helical bubbles.

3. Conclusion

This study investigates the wakefield acceleration process driven by the interaction of an LS pulse with a gaseous plasma. The results demonstrate that when the LS pulse propagates in the plasma, its unique helical intensity and phase distributions expel electrons outward in a spiral manner via the ponderomotive force, forming a bubble-like structure with a distinct 3D helical configuration. The trapped electrons are naturally aligned along the spiral bubble-like structure, forming a coherent 3D helical electron beam. Under the influence of a longitudinal electric field, electrons are continuously accelerated. Simultaneously, they are subjected to the combined effects of the transverse focusing and azimuthal electric fields, resulting in a significant OAM. Note that after the electron beam enters a vacuum, its spring-like structure and OAM remain stable. By establishing a simplified theoretical model to analyze the electric field structure inside the bubble, we found that the theoretically predicted distributions of the radial and azimuthal electric fields show excellent agreement with the results of 3D PIC simulations. This analysis reveals the crucial role of this electric field configuration in

https://doi.org/10.1017/hpl.2026.10192 Published online by Cambridge University Press

imparting OAM to electrons and clarifies the physical mechanism by which the LS-driven wakefield functions as a unique angular momentum injector.

At the same laser power, the LS pulse exhibits a higher peak intensity. As demonstrated through proton acceleration analysis, this theoretically enables a more efficient generation of high-energy electron beams. However, because of the transverse divergence of the LS pulse, its long-distance propagation in gaseous plasma presents certain challenges. Therefore, achieving higher-energy electron beams in the future will require the implementation of transverse confinement of the LS to ensure stable propagation.

Acknowledgments

We acknowledge funding from the National Natural Science Foundation of China (Grant Nos. 12475247, 12535015, 12305274).

References

1. Singh, S. K.; Krupka, M.; Krasa, J.; Istokskaia, V.; Dostal, J.; Dudzak, R.; Pisarczyk, T.; Cikhardt, J.; Agarwal, S.; Klir, D.; Rezac, K.; Giuffrida, L.; Chodukowski, T.; Rusiniak, Z.; Burian, T.; Margarone, D.; Krus, M.; Juha, L., "Hot electron emission characteristics from thin metal foil targets irradiated by terawatt laser." Laser and Particle Beams 42, e2 (2024). DOI:https://doi.org/10.1017/lpb.2023.2

2. Gonsalves, A. J. and Nakamura, K. and Daniels, J. and Benedetti, C. and Pieronek, C. and de Raadt, T. C. H. and Steinke, S. and Bin, J. H. and Bulanov, S. S. and van Tilborg, J. and Geddes, C. G. R. and Schroeder, C. B. and Toth, Cs. and Esarey, E.,, "Petawatt Laser Guiding and Electron Beam Acceleration to 8 GeV in a Laser-Heated Capillary Discharge Waveguide." Physical Review Letters 122, 084801 (2019). DOI: https://doi.org/10.1103/PhysRevLett.122.084801

3. Leemans, W. P. and Gonsalves, A. J. and Mao, H.-S. and Nakamura, K. and Benedetti, C. and Schroeder, C. B, "Multi-GeV electron beams from capillary-discharge-guided subpetawatt laser pulses in the self-trapping regime." Physical review letters 113, 245002 (2014). DOI:https://doi.org/10.1103/PhysRevLett.113.245002

4. Picksley A, Stackhouse J, Benedetti C, Nakamura K, Tsai HE, Li R, Miao B, Shrock JE, Rockafellow E, Milchberg HM, Schroeder CB, van Tilborg J, Esarey E, Geddes CGR, Gonsalves AJ. ,"Matched Guiding and Controlled Injection in Dark-Current-Free, 10-GeV-Class, Channel-Guided Laser-Plasma Accelerators." Physical Review Letters 133, 255001 (2024). DOI: https://doi.org/10.1103/PhysRevLett.133.255001

5. Miao, B. and Shrock, J. E. and Feder, L. and Hollinger, R. C. and Morrison, J. and Nedbailo, R. and Picksley, A. and Song, H. and Wang, S. and Rocca, J. J. and Milchberg, H. M.,"Multi-GeV Electron Bunches from an

https://doi.org/10.1017/hpl.2026.10192 Published online by Cambridge University Press

All-Optical Laser Wakefield Accelerator."Physical Review X 12, 031038 (2022). DOI: https://doi.org/10.1103/PhysRevX.12.031038

6. Feng, R., Qian, J., Peng, Y., Li, Y., Li, W., Leng, Y., & Li, R., “Femtosecond Infrared Optical Vortex Lasers Based on Optical Parametric Amplification.” High Power Laser Science and Engineering 10, e29(2022). DOI:https://doi.org/10.1017/hpl.2022.20

7. Zhang, X. M. and Shen, B. F. and Shi, Y. and Wang, X. F. and Zhang, L. G. and Wang, W. P. and Xu, J. C. and Yi, L. Q. and Xu, Z. Z., "Generation of intense high-order vortex harmonics." Physical Review Letters 114, 173901 (2015). DOI: https://doi.org/10.1103/PhysRevLett.114.173901

8. Zhang, H. and Zhang, L. Y. and Huang, H. T. and Wang, J. Y. and Yang, Y. J. and Tang, W. H. and Yu, T. P., "Intense vortex-laser generation and phase detection by surface plasma holograms." High Power Laser Science and Engineering 13, e2 (2025). DOI: https://doi.org/10.1017/hpl.2025.9

9. Tang, X. and Hao, J. X. and Shi, Y., "Electron Injection and Acceleration in a Twisted Laser Driven by the Light Fan." High Power Laser Science and Engineering 12, e86 (2024). DOI: https://doi.org/10.1017/hpl.2024.56

10. Shi, Y. and Zhang, X. M. and Arefiev, A. and Shen, B. F., "Advances in laser-plasma interactions using intense vortex laser beams." Sci. China Phys. Mech. Astron. 67, 295201 (2024). DOI: https://doi.org/10.1007/s11433-024-2422-2

11. Jiang, C. and Wang, W. P. and Weber, S. and Dong, H. and He, J. Z. and Sheng, Z. M. and Zhang, J., "Direct acceleration of an annular attosecond electron slice driven by near-infrared Laguerre–Gaussian laser." High Power Laser Science and Engineering 9, e44 (2021). DOI:https://doi.org/10.1017/hpl.2021.28

12. Bliokh, K. Y. and Rodríguez-Fortuño, F. J. and Nori, F. and Zayats, A. V., "Roadmap on structured waves." Journal of Optics 25, 103001 (2023). DOI:https://doi.org/10.1088/2040-8986/acea92

13. Li, Z. J. and Zhang, Y. C. and Chen, J. and Wang, L. and Feng, Y. and Wan, Y. and He, L. X. and Li, Y. F. and Zhang, J. and Zhang, J., "Unambiguous detection of high-energy vortex states via the superkick effect." Physical Review Letters 133, 265001 (2024). DOI:https://doi.org/10.1103/PhysRevLett.133.265001

14. Bu, Z. G. and Ji, Z. Y. and Yang, Y. J. and Zhang, X. M. and Shen, B. F. and Li, R. X., "Generation of quantum vortex electrons with intense laser pulses." Advanced Science 11, 2404564 (2024). DOI: https://doi.org/10.1002/advs.202404564

15. Huo, P. C. and Zhang, L. Y. and Chen, S. and Liu, C. and Shi, Y. and Yu, T. P., "Tailoring electron vortex beams with customizable intensity patterns by electron diffraction holography." Opto-Electronic Advances 7, 230184-1 (2023). DOI:https://doi.org/10.29026/oea.2024.230184

16. Guzzinati, G. and Schattschneider, P. and Bliokh, K. Y. and Nori, F. and Verbeeck, J., "Measuring the orbital angular momentum of electron beams." Physical Review A 89, 025803 (2014). DOI:https://doi.org/10.1103/PhysRevA.89.025803

https://doi.org/10.1017/hpl.2026.10192 Published online by Cambridge University Press

17. Hemsing, E. and Marinelli, A. and Reiche, S. and Rosenzweig, J. B., "Coherent optical vortices from relativistic electron beams." Nature Physics 9, 549-553 (2013). DOI:https://doi.org/10.1038/nphys2712Download citation

18. Hao, S. F.; Lv, Z. X.; Dong, H.; He, J. Z.; Huang, N. S.; Sun, F. Y.; Shi, Z. Y.; Sun, H.; Wang, W. P.; Leng, Y. X.; Li, R. X.; Xu, Z. Z., "High-gradient modulation of microbunchings using a minimized system driven by a vortex laser." Chinese Optics Letters 21, 093801 (2023). DOI:https://doi.org/10.3788/COL202321.093801

19. Hemsing, E. and Marinelli, A. and Reiche, S. and Rosenzweig, J. B., "Experimental observation of helical microbunching of a relativistic electron beam." Applied Physics Letters 100, 091104 (2012). DOI:https://doi.org/10.1063/1.3690900

20. Liu S, Li F, Zhou S, Hua J, Mori WB, Joshi C, Lu W., "A Scalable, High-Efficiency, Low-Energy-Spread Laser Wakefield Accelerator Using a Tri-Plateau Plasma Channel." Research 7, 0396 (2024). DOI: https://doi.org/10.34133/research.0396

21. Pöder, K., Wood, J. C., Lopes, N. C., Cole, J. M., Alatabi, S., Backhouse, M. P., Foster, P. S., Hughes, A. J., Kamperidis, C., Kononenko, O., Mangles, S. P. D., Palmer, C. A. J., Rusby, D., Sahai, A., Sarri, G., Symes, D. R., Warwick, J. R. & Najmudin, Z. Multi-GeV Electron Acceleration in Wakefields Strongly Driven by Oversized Laser Spots. Phys. Rev. Lett. 132, 195001 (2024). DOI:https://doi.org/10.1103/PhysRevLett.132.195001

22. Monzac, J., Smartsev, S., Huijts, J., Rovige, L., Andriyash, I. A., Vernier, A., Tomkus, V., Girdauskas, V., Raciukaitis, G., Mackevičiūtė, M., Stankevic, V., Cavagna, A., Kaur, J., Kalouguine, A., Lopez-Martens, R. & Faure, J. Optical ionization effects in kHz laser wakefield acceleration with few-cycle pulses. Phys. Rev. Res. 6, 043099 (2024). DOI:https://doi.org/10.1103/PhysRevResearch.6.043099

23. Vieira, J. and Mendonça, J. T., "Nonlinear laser driven donut wakefields for positron and electron acceleration." Physical Review Letters 112, 215001 (2014). DOI:https://doi.org/10.1103/PhysRevLett.112.215001

24. Zhang, G. B. and Chen, M. and Luo, J. and Sheng, Z. M. and Zhang, J., "Acceleration and evolution of a hollow electron beam in wakefields driven by a Laguerre-Gaussian laser pulse." Physics of Plasmas 23(3), 033112 (2016). DOI:https://doi.org/10.1063/1.4943892

25. Mendonça, J. T. and Vieira, J., "Donut wakefields generated by intense laser pulses with orbital angular momentum." Physics of Plasmas 21(3), 033107 (2014). DOI:https://doi.org/10.1063/1.4868967

26. Zhang, X. M. and Shen, B. F. and Zhang, L. G. and Wang, X. F. and Wang, W. P. and Xu, J. C. and Yi, L. Q. and Shi, Y., "Proton acceleration in underdense plasma by ultraintense Laguerre–Gaussian laser pulse." New Journal of Physics 16(12), 123051 (2014). DOI:https://doi.org/10.1088/1367-2630/16/12/123051

https://doi.org/10.1017/hpl.2026.10192 Published online by Cambridge University Press

27. Wang, X. F. and Zhang, X. M. and Shen, B. F. and Wang, W. P. and Xu, J. C. and Yi, L. Q. and Zhang, L. G. and Shi, Y., "High energy protons generation by two sequential laser pulses." Physics of Plasmas 22(4), 043117 (2015). DOI:https://doi.org/10.1063/1.4917071

28. Abedi-Varaki, M., "Analysis of plasma wakefield generation by a Laguerre-Gaussian laser beam in laser-plasma accelerators with external injection." Physica Scripta 99(9), 095611 (2024). DOI:https://doi.org/10.1088/1402-4896/ad6ebe

29. Firouzjaei, A. S. and Shokri, B., "Trapping and acceleration of hollow electron and positron bunch in a quasi-linear donut wakefield." Physics of Plasmas 24(1), 013114 (2017). DOI:https://doi.org/10.1063/1.4973598

30. Pariente, G. and Quéré, F., "Spatio-temporal light springs: extended encoding of orbital angular momentum in ultrashort pulses." Optics Letters 40(9), 2037-2040 (2015). DOI:http://dx.doi.org/10.1364/OL.40.002037

31. Guo, Y. and Liu, C. and Yang, Y. J. and Zhang, L. Y. and Wang, J. Y. and Zhang, X. M. and Yu, T. P., "Suppression of stimulated Raman scattering by angularly incoherent light, towards a laser system of incoherence in all dimensions of time, space, and angle." Matter and Radiation at Extremes 8(3), 037401 (2023). DOI:https://doi.org/10.1063/5.0136567

32. Guo, Y. and Liu, C. and Yang, Y. J. and Zhang, L. Y. and Wang, J. Y. and Zhang, X. M. and Yu, T. P., "10 GeV proton generation driven by 5 PW light spring pulses." High Power Laser Science and Engineering 12, e72 (2024). DOI:https://doi.org/10.1017/hpl.2024.72

33. Vieira, J. and Mendonça, J. T. and Quéré, F., "Optical control of the topology of laser-plasma accelerators." Physical Review Letters 121(5), 054801 (2018). DOI:https://doi.org/10.1103/PhysRevLett.121.054801

34. Arber, T. D. and Bennett, K. and Brady, C. S. and Lawrence-Douglas, A. and Ramsay, M. G. and Sircombe, N. J. and Gillies, P. and Evans, R. G. and Schmitz, H. and Bell, A. R. and Ridgers, C. P., "Contemporary particle-in-cell approach to laser-plasma modelling." Plasma Physics and Controlled Fusion 57, 113001 (2015). DOI:https://doi.org/10.1088/0741-3335/57/11/113001

https://doi.org/10.1017/hpl.2026.10192 Published online by Cambridge University Press